Research in Astronomy and Astrophysics, 24:075002 (9pp), 2024 July https://doi.org/10.1088/1674-4527/ad48d1

Toward a Direct Measurement of the Cosmic Acceleration: The Pilot Observation of HI 21 cm Absorption Line at FAST

Jiangang Kang[1,2], Chang-Zhi Lu[1,2], Tong-Jie Zhang[1,2], and Ming Zhu[3]
[1] Institute for Frontiers in Astronomy and Astrophysics, Beijing Normal University, Beijing 102206, China; tjzhang@bnu.edu.cn
[2] School of Physics and Astronomy, Beijing Normal University, Beijing 100875, China
[3] National Astronomical Observatories, Chinese Academy of Sciences, Beijing 100101, China
Received 2024 January 27; revised 2024 May 1; accepted 2024 May 5; published 2024 June 19

Abstract

This study presents results on detecting neutral atomic hydrogen (H I) 21 cm absorption in the spectrum of PKS PKS1413+13 at redshift $z = 0.24670041$. The observation was conducted by FAST, with a spectral resolution of 10 Hz, using 10 minutes of observing time. The global spectral profile is examined by modeling the absorption line using a single Gaussian function with a resolution of 10 kHz within a 2 MHz bandwidth. The goal is to determine the rate of the latest cosmic acceleration by directly measuring the redshift evolution of the H I 21 cm absorption line with Hubble flow toward a common background quasar over a decade or longer time span. This will serve as a detectable signal generated by the accelerated expansion of the Universe at redshift $z < 1$, referred to as redshift drift $\dot{z}$ or the SL effect. The measured H I gas column density in this DLA system is approximately equivalent to the initial observation value, considering uncertainties of the spin temperature of a spiral host galaxy. The high signal-to-noise ratio of 57, obtained at a 10 kHz resolution, strongly supports the feasibility of using the H I 21 cm absorption line in DLA systems to accurately measure the redshift drift rate at a precision level of around 10^{-10} per decade.

Key words: (cosmology:) cosmological parameters – cosmology: observations – cosmology: theory – (cosmology:) dark energy – radio lines: ISM – radio lines: galaxies – ISM: clouds

1. Introduction

The occurrence of the accelerated expansion of the Universe since ∼5 Gyr ago was discovered (Riess et al. 1998; Perlmutter et al. 1999). It clearly indicates the existence of new physics beyond the Standard Model. Later on, the acceleration was extensively described by a phenomenological model, called "dark energy," with the unusual equation of state parameter $w_{DE} = p_{DE}/\rho_{DE} < -1/3$, w_{DE},p_{DE} and ρ_{DE} respectively denote the state of equation (EoS), pressure and energy density of dark energy respectively. During the past two decades, massive observational experiments have been devoted to investigating the evolution law of w_{DE} with redshift by a variety of cosmological probes. Until now, most evidence seems to indicate that the unexpected behavior resulted from the simplest form of dark energy, i.e., the cosmological constant Λ, corresponding to $w_{DE} = -1$, finally shaping the standard ΛCDM cosmology (Escamilla et al. 2023; Martins et al. 2024). High precision measurements of the expansion history with various observational tools are a foremost subject in modern cosmology. Initially proposed by Sandage, the method to measure redshift variations in extragalactic objects was later refined by Loeb using Lyα forests in distant quasars. This observational technique is known as the Sandage–Loeb (SL) effect (Sandage 1962; Loeb 1998).

The redshift drift effect ($\Delta z/\Delta t$, hereafter $\dot{z}$), as the Cosmic Accelerometer, provides a high-precision method for directly observing the change in redshift of distant sources caused by the universes expansion, which offers a model-independent probe in cosmology (Martinelli et al. 2012; Cooke 2019; Eikenberry et al. 2019; Chakrabarti et al. 2022). The effect is negligible, with redshift and velocity drift for a typical galaxy at redshift $z = 1$ being close to 10^{-10} and 3 cm s^{-1} per decade respectively (Kloeckner et al. 2015), similar to gravitational accelerations in galaxies and clusters (Amendola et al. 2008; Darling 2012). However, the tiny signal, which is purely radial and cosmological, can be identified without interference from the local motions of the observer (Darling 2012). It can be immediately distinguished from the polarized drifts of proper acceleration (Zakamska & Tremaine 2005; Titov et al. 2011; Xu et al. 2012). An alternative explanation for the redshift drift interference is that the apparent acceleration, similar to stars circling a galaxy's core, can be consistently discounted regardless of its strength or direction. Therefore, the overall impact of proper motion within a gravitationally bound system on redshift drift is negligible (Phillipps 1982; Teuber 1986; Loeb 1998; Amendola et al. 2008; Lu et al. 2022).

Damped Lyα Absorber (DLA) systems, progenitors of spiral galaxies, have a characteristic H I column density of $N_{HI} \geqslant 2 \times 10^{20}$ cm^{-2} (Wolfe et al. 1986; Kanekar & Chengalur 2001; Kanekar et al. 2001; Gupta et al. 2013; Geréb et al. 2015). A great amount of DLA systems presumably will contribute to the

measurement precision of SL signal and lower the error of velocity drift σ_V. There are three main differences between intervening and associated absorptions that were concluded from Curran et al. (2016): (i) The mean associated profile is wider than the mean intervening profile; (ii) From a simple model of the H I column density distribution, the high velocity wings, often observed in associated absorption, arises from the sub-pc gas, which appears to be absent in the intervening absorbers, due to the associated absorption arising in an active galactic nucleus (AGN, including radio galaxies and quasars), where the majority of the gas is accreted into the central supermassive black hole, but intervening absorption lines seem to be in more quiescent galaxies; (iii) The consistency in the mean intervening profile widths to either side of $z \sim 1$ indicates no kinematical or thermal evolution with redshift.

The majority of cataloged DLA systems are at redshifts $z \geqslant 2$, detectable by the Sloan Digital Sky Survey (SDSS), because ultraviolet Lyα absorption lines at redshifts $z < 1.65$ are not observable with ground-based telescopes (Prochaska & Herbert-Fort 2004), yet only around 50 DLAs are at redshift $z \lesssim 1.7$ (Kanekar et al. 2009; Allison 2021). Using the H I 21 cm absorption line from DLA systems as an alternative to the Lyα line can measure redshift drift at any distance. This method also reveals more detailed insights into the early state of neutral gas in host galaxies. In the interstellar medium (ISM), neutral hydrogen exists in two stable phases: the Cold Neutral Medium (CNM) with a spin temperature of roughly 80–100 K, and the Warm Neutral Medium (WNM) at a much hotter spin temperature of about 5000–8000 K, while the temperature lies in $500 < T_s < 5000$ K as an unstable phase hosts the substantial portion of neutral ISM. Actually, the majority of the observed results for gas spin temperature is a column density-weighted harmonic average from the mixed phase ISM (Kanekar & Chengalur 2001; Kanekar et al. 2001; Koley 2023).

Redshifted 21 cm absorption lines in the spectra from strong radio sources can serve as a direct method to measure redshift drift (Carilli et al. 1992; Kanekar & Chengalur 2001; Darling 2012; Gupta et al. 2013; Yu & Zhang 2014; Geréb et al. 2015). The European Extremely Large Telescope (ELT), a 40 m class observatory equipped with a high-resolution spectrograph, aims to detect redshift signals between $z = 2$ and $z = 5$, by detecting the Lyα forests in the southern sky over a 20 yr period (Liske et al. 2008; Maiolino et al. 2013; Martins et al. 2021; Marconi et al. 2021). The forthcoming Square Kilometre Array (SKA) is set to achieve the goal by observing the H I 21 cm line emissions from galaxies and the absorption lines from DLA systems across a redshift range of approximately 1–13 (Kanekar & Briggs 2004; Abdalla et al. 2015; Kloeckner et al. 2015; Morganti et al. 2015; Staveley-Smith & Oosterloo 2015; Alves et al. 2019; Bolejko et al. 2019; Liu et al. 2020; Martins et al. 2021; Marques et al. 2023; Rocha & Martins 2023), meanwhile the CHIME (Bandura et al. 2014; Newburgh et al. 2014; Yu & Zhang 2014) has performed this experiment at intermediate redshifts. In addition, it is hopeful that FAST also can detect this signal (Nan et al. 2011; Li et al. 2018; Jiang et al. 2019). By using a combination of blind searches and targeted observations at a redshift of $z \leqslant 0.35$, it is expected to identify approximately 70 DLA systems by scanning the celestial equator for one month. Extending the observing time to one year will yield around 800 DLA systems, five years could result in 1900, and a decade-long search can obtain the detections of 2600 DLAs (Jiao et al. 2020; Hu et al. 2023).

In this study, we report the detection of the H I 21 cm absorption line from the DLA system at a redshift of $z = 0.24671 \pm 0.00001$ toward the quasar PKS PKS1413 +135. This observation was made using the ON-OFF mode of the FAST telescope for a duration of approximately 10 minutes in 2019 November (Lu et al. 2022). Exploring the flat cosmological model includes parameters such as H_0, Ω_m, $\Omega_{\rm DE}$, and the EoS for dark energy, w. This object is categorized as a BL Lac or red quasar due to its compact polarized continuum emission and relativistic jet in its line of sight (Combes et al. 2023). The host galaxy, an Sb-c type spiral galaxy, exhibits rapid changes in centimeter-scale optical emissions, particularly intense at near-infrared wavelengths (McHardy et al. 1991), which is a young radio source with a compact symmetric object (CSO) within $0\farcs01$ from the center in H-band imaging, showing a two-sided parsec-scale jet that is slightly bent, not aligned with the line of sight (Perlman et al. 1996). Moreover, Einstein's X-ray observation reveals a high H I column density of $N_{\rm HI} > 2 \times 10^{22}\,{\rm cm}^{-2}$ and significant extinction with $A_v > 30$ in soft X-ray data, indicating a gradual linear decline toward the infrared spectrum (Stocke et al. 1992; Perlman et al. 1996; Combes et al. 2023).

We assume the spin temperature of the H I gas cloud $T_{\rm spin} = 300$ K for PKS1314+135 in this work since its host galaxy resembles a normal spiral like Milky Way with the spin temperature from 250 to 400 K across the disk (Carilli et al. 1992; Dickey et al. 2009). The final task of the investigations of H I 21 cm absorption lines is to detect the redshift drift signal with FAST. These outcomes can be used to assert the rate of cosmic acceleration and rule out or place constraints on the competing candidates of dark energy and even furnish novel clues about the early evolution and formation of the spiral galaxy, and its dependence on the character of H I gas with cosmic time. The remaining paper is structured as follows: Section 2 provides a comprehensive background related to the redshift drift phenomenon and the models of cosmic acceleration, and the observation and analysis of data are described in Section 3; the measured results and comparisons with previous work are delineated in Section 4; Section 5 summarizes the findings derived from the H I 21 cm absorption to determine redshift drift signal.

Table 1
The Global Information of Five Objective DLA Systems: from First to Last Column Lists Background Source Name, the Absorber R.A. and decl., the Redshift of Background Source z_b, the Redshift of Absorber $z_{\rm DLA}$, the type of Absorber Including Intervening (I) and Associated (A), the Flux at 1.4 GHz from VLA Survey (Condon et al. 1996), Optical Depth τ and Line Width at 50% of the Absorption Peak and the Original Literature, respectively

Backgroud source	R.A. (J2000) (hh mm ss)	Decl. (J2000) (dd mm ss)	z_b	$z_{\rm DLA}$	Type	$S_{1.4\ \rm GHz}$ (Jy)	τ	FWHM (km s^{-1})	References (km s^{-1})
PKS 1413+135	14 15 58.818	+13 20 23.71	0.2467	0.246079	A	1.142	0.34	18	Carilli et al. (1992)
B2 0738+313 A	07 41 10.703	+31 12 00.23	0.6310	0.091235	I	2.051	0.08	13.4	Lane et al. (2000)
B2 0738+313 B	07 41 10.70	+31 12 00.2	0.6310	0.220999	I	2.285	0.042	8	Kanekar et al. (2001)
J094221+062334	09 42 21.98	+06 23 35.2	0.1237	0.12368	A	0.106	0.723	30	Curran et al. (2016)
J084307+453743	08 43 07.10	+45 37 42.9	0.1920	0.191 95	A	0.260	0.273	80	Geréb et al. (2015)

2. Cosmic Acceleration Model

In the comoving coordinate framework ($ds^2 = 0$), the redshift of a specific radio source over cosmic time t evolves, considering the radiation emitted by the source from t_s to $t_s + \Delta t_s$. It has been lately observed from t_0 to $t_0 + \Delta t_0$, since $\Delta t/t \ll 1$, and one can ascertain the redshift drift, where t_s is the time at which the source emitted the radiation, and t_0 is the time at the observer. Relying on the definition of Hubble parameter $H(z) = \dot{a}/a$, then redshift drift $\dot{z} = \Delta z/\Delta t$ can be defined as

$$\dot{\rm z} = H_0(1 + {\rm z}) - H({\rm z}), \tag{1}$$

where

$$H(z) = H_0\sqrt{\Omega_m(1 + z^3 + \Omega_{DE}(1 + z)^{3(1+\omega)}}, \tag{2}$$

is the Hubble parameter equation with an EoS of dark energy ω, once the contributions of cosmic radiation and curvature flatness are assumed. $H_0 = 100\,{\rm h\,km\,s^{-1}\,Mpc^{-1}}$ is the Hubble constant today. As the tracer of the expansion rate of the Universe, $\dot{\rm z} > 0$ or < 0 signifies the accelerated and decelerated expansion of the Universe, respectively, and ${\rm z} = 0$ means it is coasting (Balbi & Quercellini 2007; Jain & Jhingan 2010). Identically, the spectroscopic velocity change during an observing period Δt for a comoving object, $\Delta v \equiv c\Delta z/(1+z)$, and the frequency drift based on the of $\nu_1 = \nu_{21}/(1+z)$ and $\nu_2 = \nu_{21}/(1+z+\Delta z)$ can be read

$$\Delta\nu = \nu_2 - \nu_1 \approx -\nu_{21}\frac{\Delta z}{(1+z)^2}. \tag{3}$$

Here $\nu_{21} = 1420.405751768$ MHz for the rest frame frequency of H I 21 cm absorption line and z is the first measured redshift, ν_2 and ν_1 are the first and second observed frequency, respectively, c is the light of speed.

Figure 1 shows the redshift drift $\dot{\rm z}$ and the corresponding frequency changes $\Delta\nu$ by the timescale of 5 yr and 10 yr under the ΛCDM (Planck 2018 result, P18) cosmology (Planck Collaboration et al. 2020) and Chevallier–Polarski–Linder (CPL, $\omega_0 = -1$ and $\omega_a = -0.1$) parameterization (Chevallier & Polarski 2001; Linder 2003; Balbi & Quercellini 2007) in colored lines, respectively, and the five objective sources in

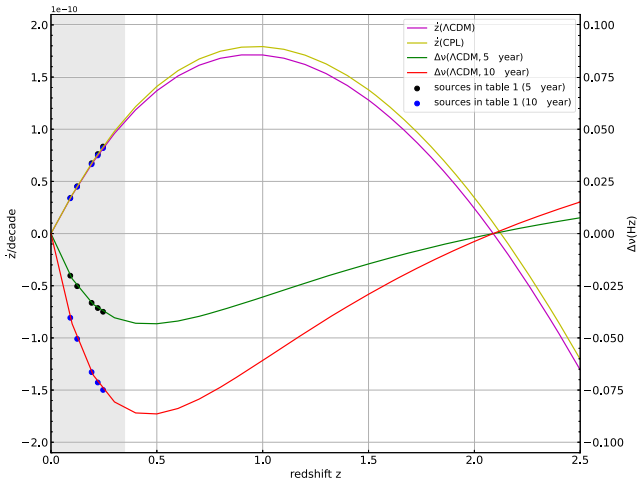

Figure 1. Theoretical redshift drift $\dot{z}$ (left) in ΛCDM (magenta) and CPL model (yellow) and the corresponding frequency change $\Delta\nu$ (right) along with redshift at the observing time period of 5 years (green) and 10 years (red) under the base ΛCDM. The five objective sources in Table 1 are marked in blue and black dots, respectively. The shallow gray region is the redshift scope that FAST covers.

Table 1 are marked in solid dots that will be observed by FAST for redshift drift experiment. Based on this figure, dark energy candidates can be effectively constrained at high redshifts using SL signal. However, distinguishing the two mainstream candidates becomes challenging at low redshifts without combining various observational data. To achieve a frequency resolution of less than 0.1 Hz for the five candidate sources listed in Table 1 within the shaded area of Figure 1, the observing period needs to be extended to 10 or 20 yr or even longer, along with the development of more advanced backend techniques to improve spectral accuracy.

Alternatively, the redshift drift effect can be quantized using the velocity drift $\dot{\rm v}$, typically a few mm s^{-1} per year. This effect is debated in alternative cosmological models with specific model parameters, highlighting the role of dark energy with energy density $\Omega_{\rm DE}$ ranging from 0 to 1 in the redshift volume $z < 2.5$ as affirmed by the results in Figure 2. The figure shows

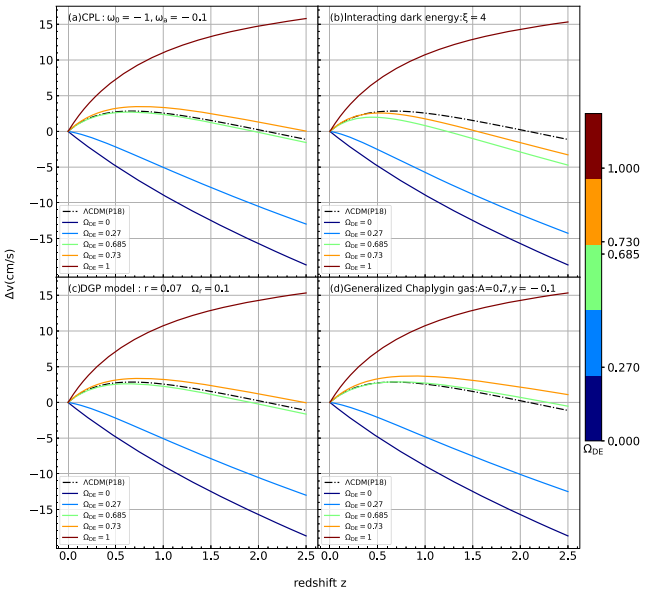

Figure 2. The evolution of velocity drift Δv as a function of redshift when the observing time-span $\Delta t = 10$ yr (year) of the same object is fixed under the four alternative cosmological models. Each colored curve signifies a certain value of $\Omega_{\rm DE}$ as the ticks on the right colorbar indicate, and the black dash-dotted stands for Δv under the ΛCDM model as the reference case.

four competing cosmological models used to predict the evolution of velocity drift $\dot{\rm v}$ with redshift z, based on changes in dark energy density $\Omega_{\rm DE}$ from 0 to 1 over a 10 yr observation period with a fixed $H_0 = 70\,{\rm km\,s^{-1}}$. Further investigation into redshift drift effects under different cosmological scenarios can be found in previous research (Balbi & Quercellini 2007; Liske et al. 2008; Esteves et al. 2021). The behavior of each model plotted $\dot{\rm v}$ from (a) to (d), with ΛCDM framework as a reference, described by the central black dash-dotted line in each panel fixing $\Omega_{\rm DE} = 0.685$. The variation of $\Omega_{\rm DE}$ ranges from 0.685 to 0.73 across panels (a)–(d), and the trajectory of Δv in the four models mimics that of ΛCDM. By observing the velocity drift $\dot{\rm v}$, the alternative cosmological models can be further differentiated, especially at high redshifts $z > 0.5$ as depicted in plots (a) to (d). For $\Omega_{\rm DE} = 0.685$ cases, the Δv in (a), (c) and (d) has a completely common tendency compared with what is in ΛCDM at redshift $z \leqslant 0.5$, and Δv in (b) is somewhat less, 0 to $1\,{\rm cm\,s^{-1}}$ than in ΛCDM from redshift $z = 0$ to 0.5. However, in the case of $\Omega_{\rm DE} = 0.73$, at redshift $z \leqslant 0.5$, the prediction of Δv in (b) mostly agrees with ΛCDM, otherwise (a), (c) and (d) uniformly are larger than 0 to $1\,{\rm cm\,s^{-1}}$, the few differences in those models cannot be the elements of the specific free parameters since they have been fixed, and the biases among these models are about to be carefully discussed with the advent of high-precision data, such as SKA and ETL. Owing to the arrangement we propose, the first five targeted sources in Table 1 will be observed, and the range of S/N can lie in 50–1000 as the current status of FAST, with experimental time spanning the periods of $\Delta t = 5$ and 10 or 20 yr and imposing exposure time limits on the source. An appreciable amount of DLA systems surely reduces the systematic error of the spectral line and enhances the measured accuracy to reinforce the reliability of the experiment.

3. Observation and Analysis

FAST conducted a 10 minutes observation of the DLA system at redshift $z = 0.24670045$ toward PKS PKS1413+135 using its 19-beam receiver in L-band to sample data from two polarizations at the central beam in ON–OFF mode (300 s in ON mode). By adding 10 K noise, the raw spectrum is obtained using the fast Fourier transform (FFT) technique, with a cut-off frequency range of 1132–1144 MHz and stored at a resolution of 10 Hz.

The top part of Figure 3 shows the temperature intensity of PKS1413+135 in Kelvins (K) at 1139.21 MHz, indicating a shallow absorption line with a temperature around 16–17 K. About 322 s of data were effective out of a total of 636 s, with the remaining 314 s of data being unstable, possibly due to instrument effects. The histogram below Figure 3 displays the probability distribution of each root mean square rms bin of raw data, illustrating four modes when outside the absorption line and RFI band. The rms level distribution on-source basically follows a Gaussian profile, with weighted rms values of 2.103×10^{-13} and 1.644×10^{-13}. However, the rms values under source-off mode are relatively diffuse, with the weighted rms being 1.371×10^{-13} and 9.06×10^{-14}, respectively, and the final signal-to-noise ratio (S/N) can be estimated based on the four rms level states. Figure 4 shows absorption lines at 1139.21 MHz with a frequency resolution of 10 Hz in source-on/diode-on and source-on/diode-off modes.

To calibrate the raw power to temperature and then to flux, we use the 322 s effective data. The 154 s with the source on and 168 s with the source off can be processed in the following manner to convert the raw data into temperature as follows

$$\begin{aligned} {\rm T_1} = T_{\rm sys}^{\rm on} &= \frac{P^{\rm on}}{P^{\rm off} - P^{\rm off}} T_{\rm cal} - T_{\rm cal}, \\ {\rm T_2} = T_{\rm sys}^{\rm off} &= \frac{P^{\rm off}}{P^{\rm on} - P^{\rm off}} T_{\rm cal}, \end{aligned} \tag{4}$$

$$\begin{aligned} w_i &= \sigma_j^2/(\sigma_1^2 + \sigma_2^2), \quad i, j = 1, 2, i \neq j, \\ T_{\rm sys} &= w_1 T_1 + w_2 T_2. \end{aligned} \tag{5}$$

In the equation, P represents the measured power, and $T_{\rm cal}$ refers to the temperature of the noise diode, which is assumed to be 10 K, while σ_1 and σ_2 stand for the rms levels for source-on and source-off, respectively. To smooth out standing waves and baseline fluctuations, we apply a Gaussian convolution

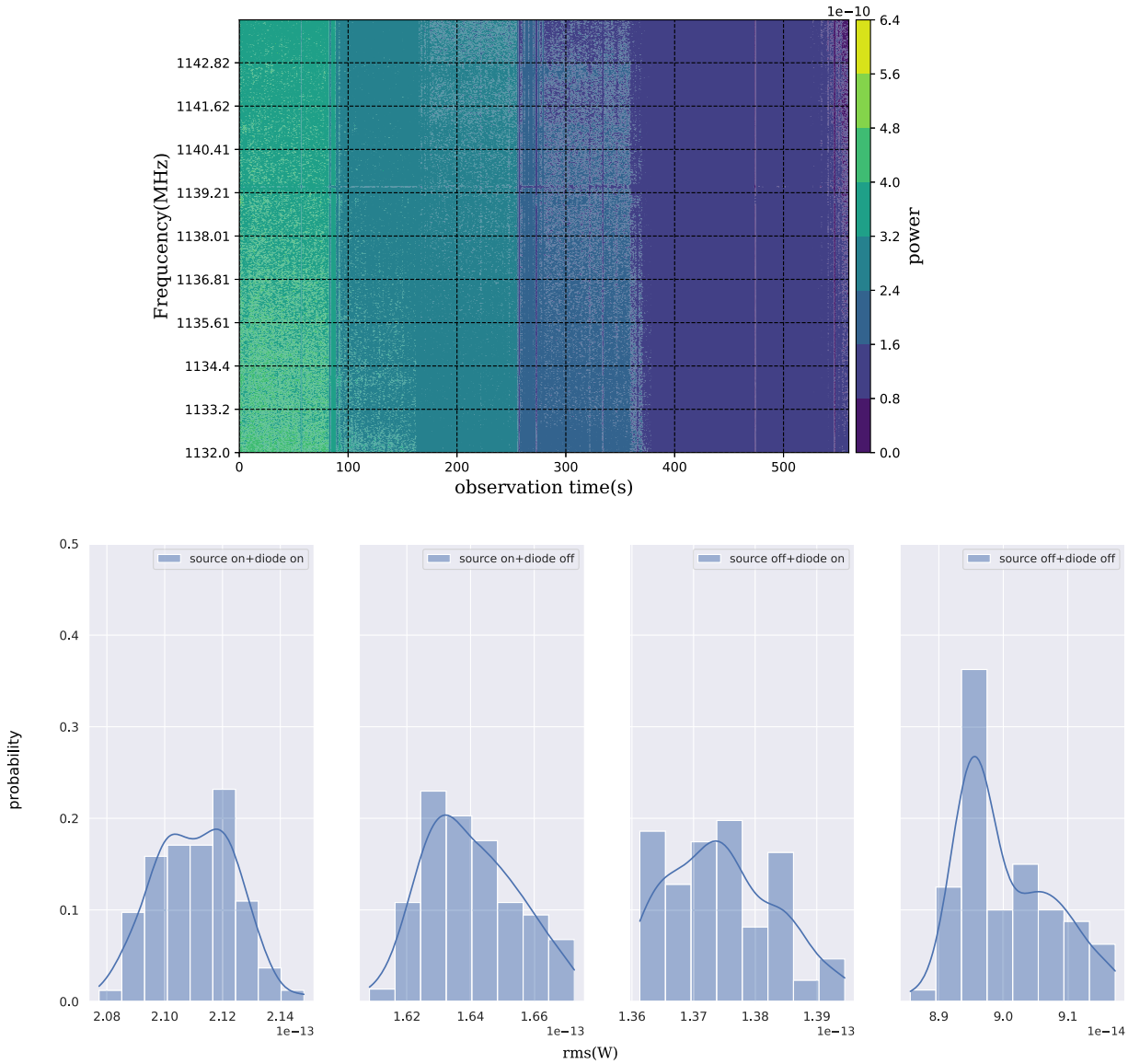

Figure 3. Top panel: the power intensity of the absorption line in the background spectrum of PKS1413+135 along with the different effective observational time of the four different observational statuses: source-ON/OFF and diode-on/off. A faint absorption line near 1139.21 MHz in the horizontal direction can be seen. The lower histogram shows the probability distribution of the rms level of the data in terms of raw data power, solid curve fits trendency of data distribution.

function with a 3σ width, except at the region of the absorption peak. Then, we correct the raw spectrum baseline by fitting a combined polynomial and sine function and remove this fitted baseline from the original data set. We analyze the absorption feature by fitting it with a single Gaussian function to determine the optical depth at the peak. Lastly, we calculate the flux density in millijanskys (mJy) by dividing it with the antenna gain factor of 16.48 K Jy^{-1}, as demonstrated in Figure 5, with a frequency resolution of 10 kHz. The equation below is used to compute the column density ($N_{\rm HI}$) and the optical depth (τ) of the DLA system (Zhang et al. 2021)

$$N_{\rm HI} = 1.823 \times \frac{T_s}{f} \int \tau dv,$$
$$\tau = -\ln\left(1 + \frac{S_{\rm HI}}{S_{1.42G}}\right). \quad (6)$$

In this context, T_s represents the H I gas spin temperature, f indicates the absorber's covering factor, which typically defaults to one, and v is the radial velocity in km s^{-1}. The

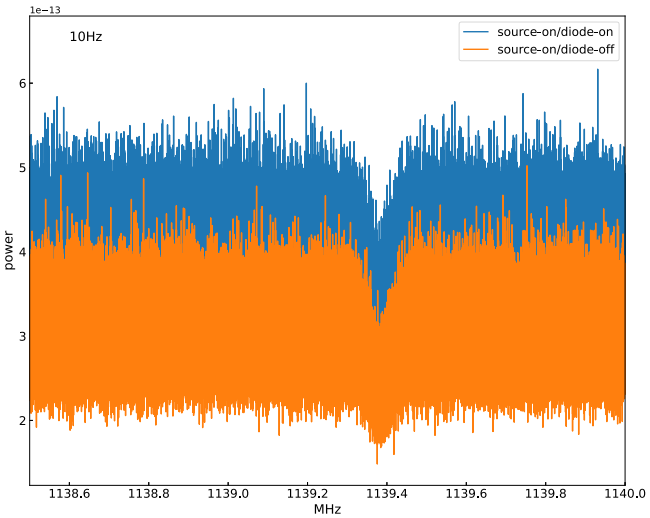

Figure 4. The power of the raw data (the PKS1413+135 source) with the raw data frequency resolution of 10 Hz with source-on-diode-on and source-on-diode-off mode. The absorption feature is clearly seen near 1139.21 MHz.

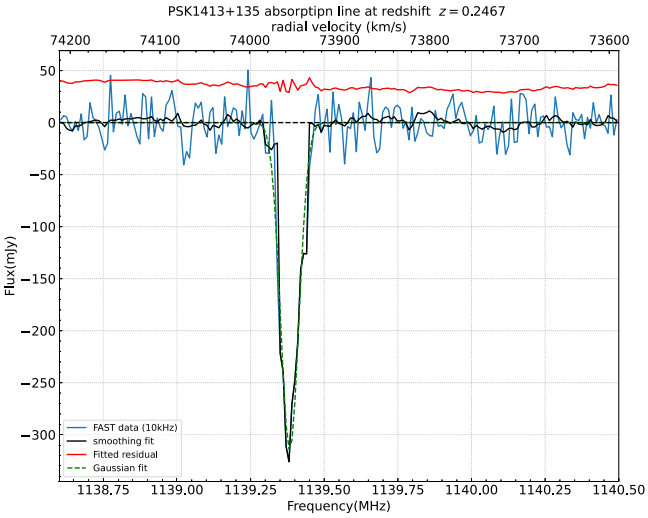

Figure 5. The H I absorption feature of PKS PKS1413+135 at the spectral resolution of 10 kHz. The light blue line represents the raw data, while the black curve is a smoothed line within a 0.5 MHz bandwidth. The green dotted line represents a single Gaussian function profile, while the red solid line shows the residual between the original data and the fit, approximately 40 mJy.

S_{HI} represents the intensity of the absorption line, indicated by a negative number, while $S_{1.4\,GHz}$ denotes the strength of the radio emission at 1420.4 MHz as recorded by the NVSS survey.[4] The S/N is calculated as the ratio of peak flux to the rms level (Kang et al. 2022)

$$S/N = \frac{F_p}{\sigma(F)}, \quad \sigma(F) = (\sigma_{rms,2} + \sigma_{rms,4})/4. \tag{7}$$

The F represents peak flux, while $\sigma(F)$ indicates the mean rms level (mJy) of the absorption line only considered in diode-off cases. $\sigma_{rms,1}$ to $\sigma_{rms,4}$ are computed by the mean of four case weighted rms, $\sigma_i = \Sigma_{Pi} \times rms_{Pi}$ as depicted by the histogram of Figure 3, and P_i labels the probability and its corresponding rms_i in each bin. To correct the heliocentric radial velocity in Astropy's coordinate module, the observed radial velocity in radio frequency ($v_m = c(\nu_0 - \nu_m)/\nu_0$) needs to be added after subtracting the baseline of the spectrum as a linear approximation (Robitaille et al. 2023), then v can be displayed as follows (Jiao et al. 2020)

$$v = v_m + v_b + \frac{v_m v_b}{c} \quad (\mathrm{km\ s^{-1}}). \tag{8}$$

In Figure 5, v represents the final radial velocity on the x-axis. ν_0 and ν_m are the rest and observed frequencies of the 21 cm line, respectively. v_b is the barycentric correction velocity based on the telescope's position on Earth at a specific observation time, and c is the speed of light in a vacuum. The barycentric correction velocity v_b for the absorption line of PKS1413+135 is $1.33\,\mathrm{km\,s^{-1}}$, with an accuracy of about $3\,\mathrm{m\,s^{-1}}$ for the source. The peak position of the absorption profile indicates the redshift drift signal of cosmic acceleration, and σ_V represents the profile's narrowness, a common method validated for single-dish FAST data (Koribalski et al. 2004; Zhang et al. 2021)

$$\sigma_V = 3\frac{\sqrt{PR}}{S}\ (\mathrm{km\ s^{-1}}). \tag{9}$$

Here, R represents velocity resolution, S stands for S/N, and w_{20} and w_{50} represent the width of the absorption line at 20% and 50% levels respectively. The parameter $P = (w_{50} - w_{20})/2$ quantifies the sharpness of the profile edges (Koribalski et al. 2004; Zhang et al. 2021). The uncertainty estimation is applied in the analysis of frequency, redshift, and velocity in Section 4.

4. Results and Discussions

The absorber was exposed for about 156 s with a frequency resolution of 10 Hz. The data were processed to show radial velocity from 73,940 to 73,970 $\mathrm{km\,s^{-1}}$ using a 10 kHz frequency resolution and the bandwidth was limited to 2 MHz as shown in Figure 5. We use a single Gaussian model to fit the absorption profile, with the best-fit parameter values displayed in Table 2. The total flux density obtained is 1053.72 ± 37 mJy, with a peak value of 338.016 ± 4.419 mJy. The column density is $N_{HI} = 2.2867 \times 10^{22}\mathrm{cm^{-2}}$, and the integrated optical depth at the peak is $\tau = 0.329 \pm 0.021$, assuming a spin temperature of $T_s = 300$ K in a spiral host galaxy. The result is in agreement with the form of $N_{HI} \simeq 1.3 \times 10^{19} \times T_s/f\ \mathrm{cm^{-2}}$, given that $f \leqslant 0.1$, indicating that the source has been well resolved (Carilli et al. 1992).

[4] https://www.cv.nrao.edu/nvss/NVSSlist.shtml

Table 2
The Parameters used to Fit the DLA in PKS1413+135 Spectra within a 2 MHz Bandwidth are All Best-fit Values Assumed to Follow a Gaussian Profile $f(x) = a \exp \frac{(x-\mu)^2}{2\sigma^2}$. The final columns indicate the velocity uncertainty σ_V

Bandwidth (MHz)	S/N	res_ν (kHz)	res_v (km s^{-1})	μ (km s^{-1})	σ (km s^{-1})	a (mJy)	σ_V (km s^{-1})
1138.0∼1140.0	57.4357	10	3.284	73 958.9408	9.3071	−55.483	0.2306

Note. The final columns indicates the velocity uncertainty σ_V.

The H I 21 cm absorption line profile in DLA systems against background radio sources shows complex spectral structures with multiple asymmetric components, reflecting the presence of unsettled gas in the ISM. This includes gas outflows from radio jets or tidal streams, as well as infalling H I gas toward central black holes in host galaxies (Kanekar et al. 2001 Roy et al. 2013; Geréb et al. 2015; Morganti & Oosterloo 2018; Hu et al. 2023), and the minor wing components are needed for precise fits, yet they are omitted from the $\dot{z}$ measurement when the S/N is sufficiently high (Carilli et al. 1992; Darling 2012). The DLA system facing PKS1315+145 features two Gaussian components within its absorption line at $z = 0.24670374$, according to the analysis (Darling 2012). Due to the brief 10 minutes observation period of this source, we were unable to clearly identify all the minute components in our analysis. As a result, it was not possible to resolve the finer structures in detail, and we had to represent the entire spectral line with a simplified Gaussian profile, which includes a significant damping wing, as depicted in Figure 5. The observed data align precisely with the Gaussian fit, resulting in a total flux of $F = 1045.747\,\mathrm{mJy} \pm 0.192$. This provides an S/N of 57.4357 at a frequency resolution of $\Delta\nu = 10\,\mathrm{kHz}$. Additionally, the barycentric radial velocity is determined to be $v = 73944.3109 \pm 0.1139\,\mathrm{km\,s^{-1}}$, with a redshift ($z$) of $0.246\,700\,21 \pm 0.0011$ and a central frequency (f) of $1139.390\,17 \pm 0.1346$ MHz. The findings align with the prior study, acknowledging some uncertainty (Carilli et al. 1992).

In reality, the data of the absorption lines have been examined as preparatory work (Lu et al. 2022). The line is resolved with frequency resolutions of 0.1, 1, and 10 kHz in three bands: 1135.0–1145.0 MHz, 1137.4–1141.4 MHz, and 1138.4–1140.4 MHz, respectively. A single Gaussian profile is used to fit the absorption feature, resulting in various S/N ranging from 8.08 to 55.43. The velocity uncertainty σ_V is at the level of 0.11 km s^{-1}. In contrast, we revisit the raw data and process them using an alternative approach represented by Equation (4) related to the H I emission method of extragalaxies. The line is modeled with a Gaussian profile as indicated in Table 2, with the fitting results displayed in the left panel of Figure 6. In Lu's study, the absorption peak is at (1139.375, −318.3) on the blue line, while in this study, it is at (1139.383, −326.9) on the orange line. The frequency has shifted by approximately 0.005 MHz and there is an 8 mJy difference in peak flux. Other quantities such as S/N, velocity error, redshift error, and the total flux of the absorber can also be calculated as their relative errors using Equation (10) as shown in the right panel. The error bars indicate a consistent decrease in error from left to right, with the error remaining below 10%. The S/N has the highest error at 8.821%, while the frequency has the least at just 0.0000004%. For clarity in the graphical representation, the error percentages for velocity and frequency have been amplified by a factor of 10,000, and for redshift by a factor of 100.

$$\mathrm{difference}(\%) = \frac{Q_T - Q_L}{Q_L}. \tag{10}$$

The equation presents the relative error for these measurements at the percent level, with T denoting this study and L indicating the results from Lu et al. (2022). The comparative differences can be seen in the chart referenced as Figure 6. In addition, as spectral resolution increases, the velocity uncertainty σ_V diminishes, leading to more accurate results due to fewer geometric distortions and more thorough processing of the initial data, according to Equation (9), which does nothing with the depth of the absorption line peak. Despite the limited observation time of the source, the baseline fluctuations and various spectral RFI noises have been successfully removed using Gaussian fitting and RFI mitigation algorithm, allowing for the clear extraction of the absorption line's global information, as shown in Figure 5. The observed radial velocity has been corrected to the heliocentric frame by applying a barycentric adjustment of 1.33 km s^{-1} using the Astropy method.

Accurately detecting the tiny redshift drift, as the indicator of cosmic acceleration, and to establish a definitive SL cosmology, it is essential to improve data accuracy. This includes meeting spectral resolution below 0.1 Hz and velocity measurement accuracy on the order of mm s^{-1}, requirements comparable to those of the SKA or ELT, along with compiling a comprehensive catalog of DLA systems and, moreover, distinguishing the unique acceleration-related pollution caused by nearby systems. FAST's spectral resolution for the SETI experiment, with an expected frequency accuracy of 3.725 Hz, actually achieved 7.5 Hz per channel (Zhang et al. 2020; Tao et al. 2022). In this case, an efficient approach to increase the

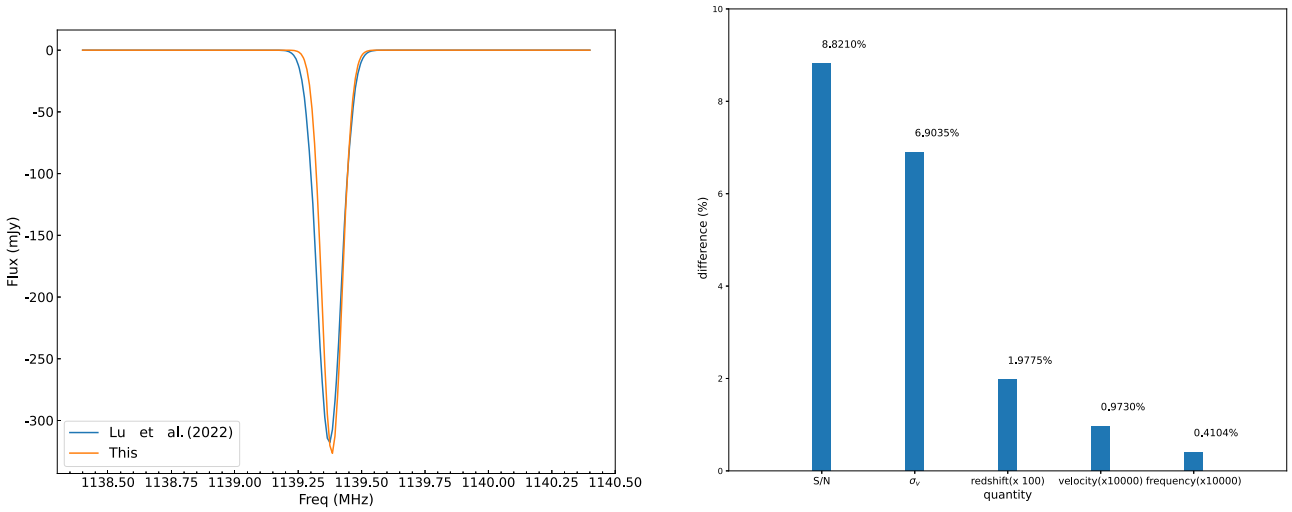

Figure 6. Left panel: The fitting comparison of H I absorption feature of PKS1413+135 in this work with the result of Lu et al. (2022), in blue and orange line respectively. Right panel: The relative errors are presented in bars in percent form of S/N, velocity error, redshift, frequency, total flux between two works, this work shows the results of the data processing.

detection of redshift drift signal is to extend the observation period of H I 21 cm absorption lines in DLA systems against the same background source. The recent release of the extensive survey of H I emission from extragalactic objects by FAST surely includes host galaxies of potential DLA candidates. These DLA system catalogs continuously either improve accuracy or relieve error of redshift drift signal via the data from H I 21 cm absorption in nearby cosmological volumes (Kang et al. 2022; Zhang et al. 2023).

5. Summary

Initially, we present the concept and framework of redshift drift as a Cosmic Accelerometer through the background of cosmological dynamics. The analysis in Figure 1 shows that a radio telescope must have a spectral resolution of less than 0.1 Hz over a 5 or 10 yr observation period to accurately detect and measure the rate of cosmic acceleration. In our next proposal, we will observe the five objective sources at various redshifts and relative information can be found in Figure 1. Furthermore, the predicted spectroscopic velocity drift $\dot{v}$ is analyzed for four alternative cosmological frameworks beyond the ΛCDM model by varying the dark energy density $\Omega_{\rm DE}$ from 0 to 1. These frameworks include CPL, interacting dark energy, DGP model, and Generalized Chaplygin gas. These models can be distinguished easily at high redshifts ($z > 0.5$), showing pretty small differences of 0–1 cm s^{-1} at lower redshifts. Utilizing high-quality redshift drift data and other cosmic probes at different scales to further research is needed. Our study centers on examining the H I 21 cm absorption line in the DLA system linked to PKS 1413+135, observed at a redshift of z=0.24670041. This observation, conducted by FAST with a spectral resolution of 10 Hz, lasted for 10 minutes. The final measurements indicate a radial velocity of $v = 73944.3109 \pm 0.1139$ km s^{-1} at the absorption line's peak, with a redshift of $z = 0.24670021 \pm 0.0011$. The central frequency is calculated to be $f = 1139.39017 \pm 0.1346$ MHz. The neutral hydrogen column density, derived from the integrated optical depth $\tau = 0.329 \pm 0.021$, is $N_{\rm HI} = 2.2867 \times 10^{22}$ cm^{-2}, assuming a spin temperature of 300 K as a spiral host galaxy. This value aligns with the expected column density formula $N_{\rm HI} = 1.3 \times 10^{19} \times (T_s/f)/{\rm cm}^2$ when considering the spin temperature's uncertainty.

The comparison of the absorption line data with the study of Lu et al. (2022) is depicted in Figure 6. The left panel shows the Gaussian fit, while the right panel presents the relative errors in S/N, velocity dispersion ($\sigma_{\rm V}$), measured redshift, velocity, and frequency. The relative errors are all below 10%, with some showing negligible discrepancies. The approach for converting raw power data into temperature, as detailed in Equation (4), yields essentially consistent results across the two different analyses. The findings confirm that using the H I 21 cm absorption line as a probe for the redshift drift effect is effective for measuring cosmic acceleration rates beyond quasar Lyman-α forests. Efforts are underway to enhance the signal's accuracy by analyzing the overall shape of the absorption profiles, applying a Gaussian function for better fit, and identifying finer spectral details to clarify the conditions and components of H I gas in host galaxy. Over a decade, by compiling over 2000 candidate DLA systems observed across various parts of the sky with FAST, SKA or ELT, we can significantly enhance the precision of the SL effect. These improvements can reach up to two orders of magnitude and achieve the required mm s^{-1} or less than 0.1 Hz precision, thus allowing us to ultimately assert the acceleration of the Universe and deepen our understanding of dark energy, using the statistical

analysis of H I 21 cm absorption lines and potentially to refine real-time cosmology.

Acknowledgments

This work is supported by the National SKA Program of China (2022SKA0110202) and the National Natural Science Foundation of China (grants No. 11929301). This work made use of the data from FAST (Five-hundred-meter Aperture Spherical Radio Telescope). FAST is a Chinese national mega-science facility, operated by the National Astronomical Observatories, Chinese Academy of Sciences.

References

Abdalla, F. B., Bull, P., Camera, S., et al. 2015, in Proc. of Advancing Astrophysics with the Square Kilometre Array (AASKA14)
Allison, J. R. 2021, MNRAS, 503, 985
Alves, C. S., Leite, A. C. O., Martins, C. J. A. P., Matos, J. G. B., & Silva, T. A. 2019, MNRAS, 488, 3607
Amendola, L., Balbi, A., & Quercellini, C. 2008, PhLB, 660, 81
Balbi, A., & Quercellini, C. 2007, MNRAS, 382, 1623
Bandura, K., Addison, G. E., Amiri, M., et al. 2014, Proc. SPIE, 9145, 20
Bolejko, K., Wang, C., & Lewis, G. F. 2019, arXiv:1907.04495
Carilli, C. L., Perlman, E. S., & Stocke, J. T. 1992, ApJL, 400, L13
Chakrabarti, S., Gonzalez, A. H., Eikenberry, S., et al. 2022, arXiv:2203.05924
Chevallier, M., & Polarski, D. 2001, IJMPD, 10, 213
Combes, F., Gupta, N., Muller, S., et al. 2023, A&A, 671, A43
Condon, J. J., Cotton, W. D., Greisen, E. W., et al. 1996, ADIL
Cooke, R. 2019, MNRAS, 492, 2044
Curran, S. J., Duchesne, S. W., Divoli, A., & Allison, J. R. 2016, MNRAS, 462, 4197
Darling, J. 2012, ApJ, 761, L26
Dickey, J. M., Strasser, S., Gaensler, B. M., et al. 2009, ApJ, 693, 1250
Eikenberry, S., Gonzalez, A., Darling, J., et al. 2019, BAAS, 51, 137
Escamilla, L. A., Giarè, W., Di Valentino, E., et al. 2023, JCAP, 2024, 44
Esteves, J., Martins, C. J. A. P., Pereira, B. G., & Alves, C. S. 2021, MNRAS, 508, L53
Geréb, K., Maccagni, F. M., Morganti, R., & Oosterloo, T. A. 2015, A&A, 575, A44
Gupta, N., Srianand, R., Noterdaeme, P., Petitjean, P., & Muzahid, S. 2013, A&A, 558, A84
Hu, W., Wang, Y., Li, Y., et al. 2023, A&A, 675, A40
Jain, D., & Jhingan, S. 2010, PhLB, 692, 219
Jiang, P., Yue, Y., Gan, H., et al. 2019, CPMA, 62, 959502
Jiao, K., Zhang, J.-C., Zhang, T.-J., et al. 2020, JCAP, 2020, 054
Kanekar, N., & Briggs, F. H. 2004, NewAR, 48, 1259
Kanekar, N., & Chengalur, J. N. 2001, A&A, 369, 42
Kanekar, N., Ghosh, T., & Chengalur, J. N. 2001, A&A, 373, 394
Kanekar, N., Prochaska, J. X., Ellison, S. L., & Chengalur, J. N. 2009, MNRAS, 396, 385
Kang, J., Zhu, M., Ai, M., Yu, H., & Sun, C. 2022, RAA, 22, 065019
Kloeckner, H. R., Obreschkow, D., Martins, C., et al. 2015, in Proc. of Advancing Astrophysics with the Square Kilometre Array (AASKA14)
Koley, A. 2023, PASA, 40, e046
Koribalski, B. S., Staveley-Smith, L., Kilborn, V. A., et al. 2004, AJ, 128, 16
Lane, W. M., Briggs, F. H., & Smette, A. 2000, ApJ, 532, 146
Li, D., Wang, P., Qian, L., et al. 2018, IMMag, 19, 112
Linder, E. V. 2003, PhRvL, 90, 091301
Liske, J., Grazian, A., Vanzella, E., et al. 2008, MNRAS, 386, 1192
Liu, Y., Zhang, J.-F., & Zhang, X. 2020, EPJC, 80, 304
Loeb, A. 1998, ApJL, 499, L111
Lu, C.-Z., Jiao, K., Zhang, T., Zhang, T.-J., & Zhu, M. 2022, PDU, 37, 101088
Maiolino, R., Haehnelt, M., Murphy, M. T., et al. 2013, arXiv:1310.3163
Marconi, A., Abreu, M., Adibekyan, V., et al. 2021, Msngr, 182, 27
Marques, C. M. J., Martins, C. J. A. P., & López, B. G. 2023, MNRAS, 527, 9918
Martinelli, M., Pandolfi, S., Martins, C. J. A. P., & Vielzeuf, P. E. 2012, PhRvD, 86, 123001
Martins, C. J. A. P., Alves, C. S., Esteves, J., Lapel, A., & Pereira, B. G. 2012, arXiv:2110.12242
Martins, C. J. A. P., Cooke, R., Liske, J., et al. 2024, ExA, 57, 5
McHardy, I. M., Abraham, R. G., Crawford, C. S., et al. 1991, MNRAS, 249, 742
Morganti, R., & Oosterloo, T. 2018, A&ARv, 26, 4
Morganti, R., Sadler, E. M., & Curran, S. 2015, in Proc. of Advancing Astrophysics with the Square Kilometre Array (AASKA14)
Nan, R., Li, D., Jin, C., et al. 2011, IJMPD, 20, 989
Newburgh, L. B., Addison, G. E., Amiri, M., et al. 2014, Proc. SPIE, 9145, 18
Perlman, E. S., Carilli, C. L., Stocke, J. T., & Conway, J. 1996, AJ, 111, 1839
Perlmutter, S., Turner, M. S., & White, M. 1999, PhRvL, 83, 670
Phillipps, S. 1982, ApL, 22, 123
Planck Collaboration, Aghanim, N., Akrami, Y., et al. 2020, A&A, 641, A6
Prochaska, J. X., & Herbert-Fort, S. 2004, PASP, 116, 622
Riess, A. G., Filippenko, A. V., Challis, P., et al. 1998, AJ, 116, 1009
Robitaille, T., Tollerud, E., Aldcroft, T., et al. 2023, astropy/astropy: v5.2.2, Zenodo doi:10.5281/zenodo.7779475
Rocha, B. A. R., & Martins, C. J. A. P. 2023, MNRAS, 518, 2853
Roy, N., Kanekar, N., & Chengalur, J. N. 2013, MNRAS, 436, 2366
Sandage, A. 1962, ApJ, 136, 319
Staveley-Smith, L., & Oosterloo, T. 2015, in Proc. of Advancing Astrophysics with the Square Kilometre Array (AASKA14)
Stocke, J. T., Wurtz, R., Wang, Q., Elston, R., & Jannuzi, B. T. 1992, ApJL, 400, L17
Tao, Z.-Z., Zhao, H.-C., Zhang, T.-J., et al. 2022, AJ, 164, 160
Teuber, J. 1986, ApL, 25, 139
Titov, O., Lambert, S. B., & Gontier, A.-M. 2011, A&A, 529, A91
Wolfe, A. M., Turnshek, D. A., Smith, H. E., & Cohen, R. D. 1986, ApJS, 61, 249
Xu, M., Wang, G., & Zhao, M. 2012, SCPMA, 55, 329
Yu, H.-R., Zhang, T.-J., & Pen, U.-L. 2014, PhRvL, 113, 113
Zakamska, N. L., & Tremaine, S. 2005, AJ, 130, 1939
Zhang, B., Zhu, M., Wu, Z.-Z., et al. 2021, MNRAS, 503, 5385
Zhang, C.-P., Zhu, M., Jiang, P., et al. 2023, SCPMA, 67, 22
Zhang, Z.-S., Werthimer, D., Zhang, T.-J., et al. 2020, ApJ, 891, 174